Available online at www.sciencedirect.com
SCIENCE DIRECT®
International Journal of Heat and Mass Transfer 47 (2004) 5219–5234
International Journal of HEAT and MASS TRANSFER
www.elsevier.com/locate/ijhmt

Transient thermal structure, turbulence, and heat transfer in a reattaching slot jet flow

V. Narayanan [a,*], J. Seyed-Yagoobi [b], R.H. Page [c]

[a] Department of Mechanical Engineering, Oregon State University, 204 Rogers Hall, Corvallis, OR 97331-6001, USA
[b] Mechanical, Materials, and Aerospace Engineering Department, Illinois Institute of Technology, 10 W. 32nd Street, Chicago, IL 60616, USA
[c] Department of Mechanical Engineering, Texas A&M University, MS 3123, College Station, TX 77843-3123, USA

Received 22 December 2003; received in revised form 25 June 2004

Abstract

The role of turbulent fluctuations on mean heat transfer coefficient in a reattaching slot jet flow is studied experimentally. Convective heat transfer rate and near-wall fluid flow are examined in the recirculation, reattachment, and post-reattachment regions for two nozzle-to-surface spacings of 0.25 and 0.75 times the width of the nozzle bottom plate. In the reattachment region, results indicate a strong correspondence between variances of near-wall velocity fluctuation and peak heat transfer rate for both spacings. Thermal structures that vary in the spanwise direction are identified in the recirculation region from low-frequency transient infrared thermographs of the heated surface. While these thermal structures are confined to regions in the vicinity of nozzle bottom plate for the low nozzle spacing, they span the entire recirculation region at larger spacings. Thermal streaks are observed past reattachment for the larger nozzle spacing, suggesting a periodic breakup and re-formation of the jet curtain. The scaling of heat transfer distribution is affected by the flow structure in the geometrically non-similar area of the recirculating flow beneath the nozzle. A correlation for peak Nusselt number is presented.

Keywords: Slot jet; Reattachment; Turbulence; Transient temperature; Heat transfer

1. Introduction

Impinging jets are used widely in industrial applications to heat, cool, or dry surfaces. Typical applications include cooling of electronic components, glass, and metals; drying of tissue, paper, and food products; and internal cooling of turbine blades. Literature on submerged impinging jets is numerous and has been periodically summarized in reviews such as those by Martin [1] and Viskanta [2]. Several nozzle configurations have been proposed over the past five decades in an effort to passively augment the transport characteristics of conventional circular and slot jets by enhancement of flow turbulence, and consequently, heat transport. For example, researchers have studied swirling jets [3], elliptic jets [4] and reattachment jets [5–7].

* Corresponding author. Tel.: +1 541 737 7012; fax: +1 541 737 2600.
E-mail address: vinod.narayanan@oregonstate.edu (V. Narayanan).

0017-9310/$ - see front matter © 2004 Elsevier Ltd. All rights reserved.
doi:10.1016/j.ijheatmasstransfer.2004.06.016

Nomenclature

b	nozzle exit opening (m)
C_p	pressure coefficient, $C_p = \dfrac{\Delta P_m - \Delta P_{m,\mathrm{ref}}}{0.5\rho V_{mo}^2}$
h	heat transfer coefficient (W/m^{2}K), $h_{\mathrm{loc}} = \dfrac{q''_{\mathrm{net}}}{T_{\mathrm{h}} - T_{\mathrm{ad}}} = \dfrac{((q_{\mathrm{elec}} - q_{\mathrm{Cu}})/A_{\mathrm{foil}}) - (q''_{\mathrm{rad}} + q''_{\mathrm{nc}})}{T_{\mathrm{h}} - T_{\mathrm{ad}}}$
k	thermal conductivity (W/m K)
Nu	Nusselt number, $Nu = \dfrac{h_{\mathrm{loc}}\lambda}{k}$
P	pressure (Pa)
q''	heat flux (W/m^2)
Re	Reynolds number, $Re = \dfrac{V_{mo}D_{\mathrm{h}}}{\nu}$
SR	image scan rate (frames/s)
T	temperature (°C)
$\overline{T}$	temporal and spatial mean temperature (°C)
U	time-averaged local velocity in the x-direction (m/s)
$\langle uu \rangle$	variance of normal velocity fluctuation in x-direction (m/s)^2
V	time-averaged local velocity in the y-direction (m/s)
$\langle vv \rangle$	variance of normal velocity fluctuation in the y-direction (m/s)^2
X_{w}	width of the nozzle bottom plate (m)
x	streamwise coordinate along the minor axis of the nozzle; $x = 0.0$ corresponds to the projected nozzle major axis on the impingement surface (m)
Y_{n}	nozzle-to-surface spacing measured from the surface to the centerline of the jet exit (m)
y	normal (vertical) co-ordinate; $y = 0.0$ location corresponds to the impingement surface (m)
z	spanwise coordinate along the major axis of the nozzle; $z = 0.0$ location corresponds to the projected nozzle minor axis on the impingement surface (m)

Greek symbols

Δ	differential
λ	length scale (m)
θ	non-dimensional RMS temperature fluctuation

Subscripts

ad	adiabatic
h	heated
i	time index (0–1648)
j	z-direction spatial index
loc	local
m	mean value (in a volume, mass, or temporal context)
nc	natural convection
o	nozzle exit
r	reattachment
rad	radiation
ref	reference value of quantity
RMS	root mean square
t	time

The slot jet reattachment (SJR) nozzle studied here was proposed as a simple geometrical modification over existing slot nozzles. It is based on the principle of flow separation at the nozzle exit and attachment onto a closely placed surface. The radial jet reattachment (RJR) nozzle, an axisymmetric counterpart to the SJR nozzle, has been studied quite extensively, both analytically and experimentally (see, for example [5–9]). The flowfield and heat transfer in steady and fully pulsed RJR nozzles was studied by Bremhorst and Agnew [10]. Reattachment nozzles find growing use in process applications for transport of heat and moisture from fragile surfaces [11]. They provide distinct advantages over conventional geometries such as circular and slot nozzles and orifices with regard to the ability to obtain high transport rates at a reduced average surface pressure.

An offset jet [12–14] represents the most relevant nozzle configuration to the SJR nozzle. Pelfrey and Liburdy have studied the mean flow structure [12] and turbulence [13] of this jet with an offset ratio of 7 and an aspect ratio of 12 using a 1-D laser Doppler anemometer (LDA). Curvature was found to cause a reduction in streamwise and an increase in normal turbulence on the stable concave side (along the dividing streamline) of the jet, while an opposite trend was observed in the unstable upper shear layer. Nasr and Lai [14] experimentally studied the flow field of a 2.25 offset ratio jet using a 2-D LDA system, and compared their results to the predictions of three turbulence models. They concluded that while all turbulence models qualitatively predicted the flow, the k–ε model best agreed with the experimental values. They also highlighted, by means of static pressure measurements, the significance of using side confinement surfaces to enhance the two-dimensionality of the jet. The attachment location, as determined from the location of peak wall pressure was found to occur at a further downstream location, and the magnitude of wall pressure was lower for the unconfined jet.

The flow over a backward-facing-step shares several similarities with the present flow geometry, such as flow separation at a distinct edge, curvature of the jet path, flow entrainment and recirculation. Early studies on this geometry have been summarized in Eaton and Johnston [15]. In their combined study of heat transfer and fluid

mechanics in a backward-facing-step geometry, Vogel and Eaton [16,17] used the reattachment distance along the impingement plate, x_r, to scale the downstream locations. Kumada et al. [18] proposed a generalized correlation for stagnation point Nusselt number in terms of an approach *Re* number and jet path length for impingement and reattachment jets. Abe et al. [19] numerically predicted the flow over a backstep with a modified k–ε turbulence model that utilized the Kolmogorov velocity scale to calculate the model functions for near-wall and low-Reynolds number effects. Le et al. [20] studied a low Reynolds number ($Re_H = 5100$) backstep flow using direct numerical simulation (DNS). The results of the simulations were corroborated by the experiments performed by Jovic and Driver [21].

Fig. 1(a) shows a cross-sectional schematic of the SJR flow field, identifying the flow parameters and zones relevant to this study. Fig. 1(b) shows details of the SJR nozzle geometry. In the SJR flow, the jet exits parallel to, and attaches on the surface along the major and minor axes. Thus, the recirculating flow on both sides of the major axis ($x = 0.0$) interact with each other beneath the bottom plate of the nozzle. An additional complexity arises from the unconfined circular ends of the SJR configuration, which causes a radial flow reattachment to occur at the ends. The circular ends, which help to maintain the sub-atmospheric recirculation region, are an important aspect of this unconfined jet geometry. An unconfined jet was studied here since it is the most practical geometry for use in a process application, where the nozzle needs to be located away from the impingement surface.

Narayanan et al. [22] studied experimentally, the heat transport rates provided by a 7.6:1 aspect ratio SJR nozzle flow and generalized local heat transfer data. Nusselt number increased with an increase in non-dimensional nozzle-to-surface spacing, Y_n/b, when the jet path from the point of separation at the nozzle exit to the location of peak heat transfer was used as the characteristic length scale. Since it was not possible to determine the actual jet path in the absence of detailed flow field measurements, a convenient straight-line approximation of this path, λ,

$$\lambda = \sqrt{Y_n^2 + \left\{x_r - \frac{X_w}{2}\right\}^2} \tag{1}$$

was chosen to represent the length scale. The location of peak heat transfer for the 7.6:1 aspect ratio SJR nozzle was found to be essentially constant when the distance

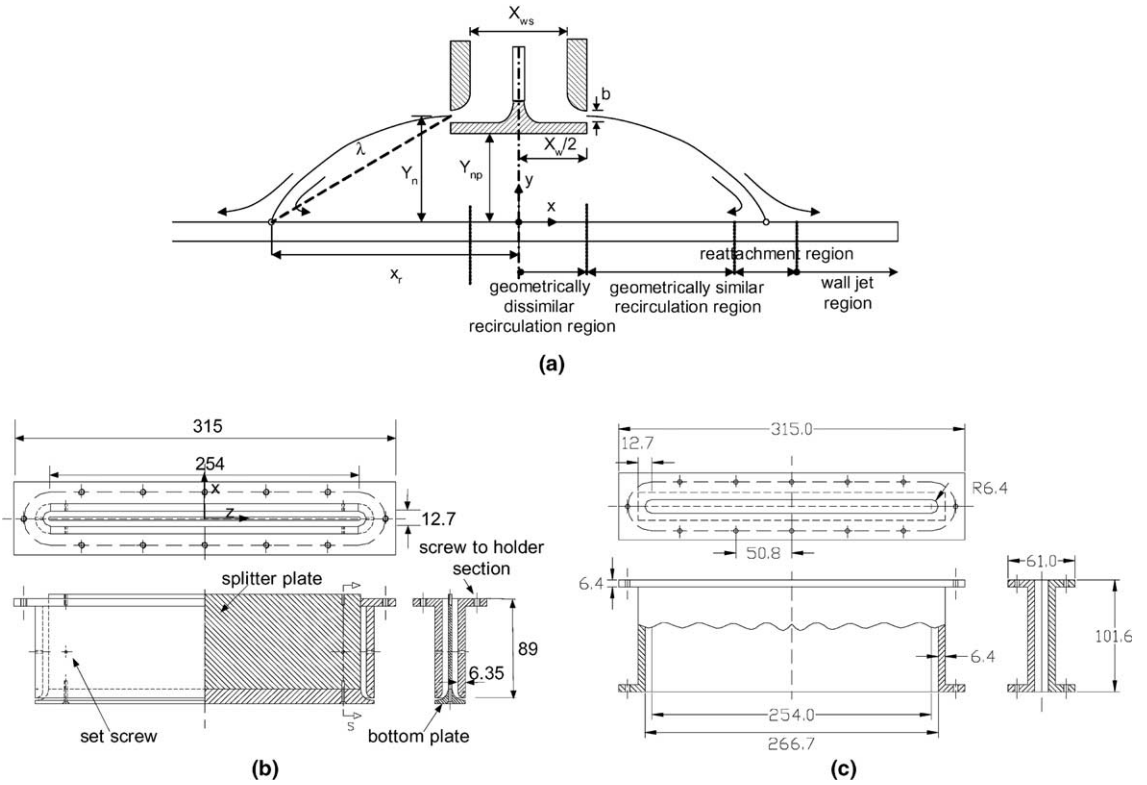

Fig. 1. (a)–(c) SJR geometry and test section details (all dimensions are in mm). (a) SJR flow field schematic identifying the pertinent geometrical parameters; (b) Geometry of the SJR nozzle; (c) Geometry of the transition slot.

from the nozzle centerline in the positive direction along minor axis, x, was non-dimensionalized with respect to the above characteristic length,

$$x_r^* = \frac{x_r - X_w/2}{\lambda} = 0.933 \quad (2)$$

This allowed for a representation of local Nu distribution as a function of x^*, Y_n/b, and Re, where x^* was defined in a manner similar to Eq. (2) for the positive x-direction,

$$x^* = \frac{x - X_w/2}{\lambda} \quad (3)$$

Heat transfer rate data and mean surface pressure measurements were reported at the nozzle centerline along the minor axis ($z/X_w = 0.0$), and the flow was treated to be two-dimensional at the centerline. Surface temperature inside the recirculation region near the bottom plate, where heat transfer rates are low, could not be obtained in their study due to limitations of the experimental apparatus.

The major objective of this study is to compare and contrast the near-wall turbulent flow structure and heat transfer of the SJR flow at two spacings: one very close to the surface at $Y_n/X_w = 0.25$, and the other farther away from the surface at $Y_n/X_w = 0.75$, for a fixed Re of 10,500 and nozzle opening, b/X_w of 0.10. The intent is to identify mechanisms for heat transport in the regions of flow identified in Fig. 1(a), with a particular emphasis on the recirculation and reattachment regions. A second objective is to provide more detailed heat transfer data, especially in the recirculation region of the flow. The quantities presented in this paper include the near-wall normal and cross-velocity fluctuation variances, $\langle uu \rangle$ and $\langle vv \rangle$, time-mean spatially local impingement surface temperature, temporal surface temperature fluctuations at specific x = constant locations on the impingement surface, mean surface pressure, and RMS averaged surface pressure fluctuations. The heat transfer data are analyzed for three turbulent Re of 5000, 10,000, and 15,000, for four nozzle spacings from $Y_n/X_w = 0.25$ to 1.00, and three exit openings from $b/X_w = 0.05$ to 0.15.

2. Experimental apparatus and procedure

The jet impingement facility was identical to the one used for slot jet studies presented in Narayanan et al. [23]. Two dedicated screw compressors located in a separate room supplied compressed air for the jet flow. The air was dried, filtered, and directed into a plenum through two settling tanks and pressure regulators. The mass flow rate was measured with a sonic nozzle at the exit of the last settling tank. The plenum consisted of a honeycomb flow straightener, followed by a series of screens and a convergent section. The plenum and impingement plate set-up were located in a large test chamber that prevented stray light and other disturbances from affecting the measurements. The flow exited the plenum through an end plate consisting of seven contoured slots of aspect ratio 20:1 of which only the central slot was used in this study.

2.1. Nozzle geometry

The SJR nozzle, shown schematically in Fig. 1(b), consisted of an 89-mm long, 254 mm × 12.7 mm cross-section slot with circular ends of 12.7 mm diameter internally. A 102-mm long transition slot section, shown in Fig. 1(c), was attached to the central slot contour on plenum end plate and preceded the SJR nozzle. The aspect ratio of the slot and SJR, determined after excluding the circular ends, was 20:1. The nozzle wall thickness was 6.35 mm. The nozzle bottom plate and inner wall of the nozzle exit were contoured along the perimeter to ensure that the jet exited the nozzle parallel to the impingement surface. A central splitter plate was used to attach the nozzle bottom plate to the main body of the nozzle. It also served to guide the flow inside the nozzle with minimal disturbance. The splitter plate was attached by means of two bullet-headed screws onto a holder section that was located between the slot and nozzle sections. The exit opening could be varied by stacking a desired number of 0.254 mm spacers between the holder section and the splitter plate. Six set screws were provided at various locations along the nozzle to precisely locate the bottom plate with respect to the slot. The exit opening was measured using precision gage blocks, and was found to be uniform to within ±0.1 mm all around. The entire assembly consisting of the holder plate, SJR nozzle, and bottom plate were attached to the transition slot section.

2.2. Heat transfer test section

A schematic of the heat transfer test section is shown in Fig. 2. The heat transfer impingement surface consisted of a central constant heat flux surface surrounded by Plexiglas end plates on all sides. The entire test section was 63.5 cm long × 63.5 cm wide. The central heated section consisted of a 0.0254-mm thick inconel alloy 600 foil 38.1 cm long × 38.1 cm wide that was stretched tightly between two solid copper bus bars. The foil was electrically heated by means of a high current DC power supply. Solid copper rods were used to transmit power to the bus bars. Voltage across the foil was measured at the bus bars. Current through the foil was measured at the power supply readout. The underside of the foil and the surrounding Plexiglas surface was coated with flat-black paint to provide a constant high-emissivity, diffuse surface for radiation detection. The

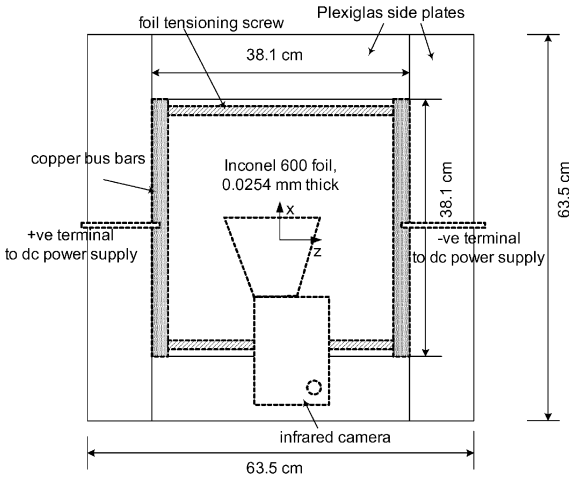

Fig. 2. Schematic of the heat transfer test section.

emissivity of the painted side of the foil was determined to be 0.96, based on ambient temperature calibration of the IR camera with respect to a calibrated thermistor located on the foil surface. The average thickness of the paint coating was measured to be 25 μm. For the present experiments, variation of emissivity with temperature was considered negligible, since the foil was heated to less than 15 °C above ambient temperature. The IR camera was placed horizontally in a vented enclosure directly below the foil, and a mirror was used to visualize the painted surface of the foil.

2.3. Instrumentation and experimental procedure

Local surface temperatures were measured non-intrusively with a 8–13 μm wavelength IR camera (Mikron Inc., model 6T62 thermotracer). The system consisted of a single cooled HgCdTe detector with front end optics that scanned the target sequentially in the z- and x-directions for radiated IR energy. In this paper, a frame refers to one complete thermal image, with 256×206 temperature data points. The maximum scan rate was 1 frame/s. The imager could be operated in two modes: (1) a normal mode, in which a two-dimensional spatial region corresponding to 256×206 physical locations were scanned for each frame, and (2) a time trace mode, in which the x-direction scanning of the imager was disabled, thereby permitting a scan across a single c = constant line over 206 equal time intervals for each frame. In the former mode, the camera was operated at its maximum signal-to-noise ratio, which provided only time-averaged surface temperature distribution. In the latter mode, temperatures could be recorded at a frame rate (or an equivalent line scan rate) ranging from 0.017 frames/s (3.45 Hz per line) to 1 frames/s (207 Hz per line). The imager had a maximum temperature resolution of 0.025 °C.

During a typical heat transfer experiment, eight consecutive temperature maps of the unheated foil with jet impingement were obtained at steady state at the highest imager signal-to-noise ratio and averaged, in order to estimate the mean local unheated foil temperature. The foil was then heated and the temperature distribution measured after steady state temperature was attained. The temperature rise in the enclosure did not exceed 1 °C during the test duration of approximately 5 h. Again, eight consecutive frames were averaged to obtain a mean local heated temperature distribution on the foil. The net heat flux removed by forced convection was estimated from the electrical energy input to the foil after correcting for electrical contact resistance, heat loss by natural convection and radiation from the upper and lower surfaces, and heat loss to the copper bus bars. The local heat transfer coefficient was determined using the net heat flux and the temperature difference between the heated and unheated foil at each location.

For transient temperature measurements along a user-specified line, the camera was operated in the time trace mode, at frame rates (equivalent line scan rates) of 0.017 frames/s (3.45 Hz), 0.05 frames/s (10.35 Hz), and 0.10 frames/s (20.70 Hz) to obtain temporal variations in surface temperature along the chosen line. In each case, eight frames of data were collected in the imager memory before being transferred to the computer. Thus, 1648 data points of transient temperature were recorded at discrete time intervals for every pixel along the z-direction. Instantaneous temperatures were subtracted from a spatial and temporal mean image temperature, $\overline{T}$, to provide the instantaneous differential temperature value, $\Delta T_{i,j}$ at each pixel along the line,

$$\Delta T_{i,j} = T_{i,j} - \overline{T} \tag{4}$$

The non-dimensional RMS temperature fluctuation at each spatial location, j, along the z-axis was calculated as

$$\theta_j = \frac{1}{\overline{T}_j}\sqrt{\frac{\sum_{i=1}^{i=n}(T_{i,j} - \overline{T}_j)^2}{n-1}} \tag{5}$$

where n corresponded to 1648 points in the thermal time-trace series, and $\overline{T}_j$ was the average temperature at that j-location. The frequency response of the foil and paint coating was determined from a numerical solution of one-dimensional transient heat conduction equation subjected to a step change in temperature at the top surface and natural convection at the bottom surface. Results indicated that the frequency response was 200 Hz for the inconel foil in the absence of the

paint coating, while a paint layer of the same thickness as the foil resulted in a much lower response of 15 Hz. Thus, the maximum detectable frequency was limited by the paint coating on the foil, and not by the imager frame rate. In estimating the frequency response with the paint layer, the thermal properties of silica were used.

Mean flow field and turbulence measurements were performed using a 1-D LDA system (TSI Inc). The mean and variance of fluctuating velocity were resolved using a component resolution technique [24]. Velocity and directional bias errors were reduced by performing a transit time weighting and by frequency shifting respectively. Mean and fluctuating surface pressures were measured using a piezo-resistive pressure transducer (Kulite Semiconductor Products, Inc., model XCS062). The transducer, amplifier, and data acquisition board were calibrated as a single unit in the range of measurement using a micro-manometer as the reference. Although the response of the pressure transducer was linear, base readings (with no air flow) taken prior to the experimental run and after the experimental run exhibited a slight zero drift. This introduced an uncertainty in the mean pressure measurements alone, since the ac values were high pass filtered prior to data acquisition. In order to account for the zero drift, two (base) pressure measurements were obtained with no flow for each experiment—the first prior to the experiment, and the second on completion of the experiment. The pressure measurements at each location were subtracted from these base readings, and the mean of the two readings was taken to be indicative of the pressure differential at that location. This method of taking a difference in voltages between the measured location and the base also eliminated any zero voltage offset of the transducer recorded under no flow condition. Typical resolution for the mean pressure measurements with the multimeter was as high as 0.08% of the maximum measured pressure.

3. Results and discussion

3.1. Preliminary verification and uncertainty estimates

Preliminary measurements of the free jet exit profile recorded at a location of $x/b = 0.26$ ($x/X_w = 0.025$, $b = 2.48$ mm) indicated a uniform mean exit velocity profile along the span wise direction between $z/X_w = \pm 4$ from the centerline, $z/X_w = 0.0$. The RMS streamwise turbulence intensity at the exit at $z/X_w = 0.0$ was 5% of the mean exit velocity, and increased by 1% from $z/X_w = 0.0$ to 4.0. Measurements of mean streamwise velocity of a free slot jet [23] at three downstream locations of $x/b > 20$ corresponded closely to the semi-analytical profile of Göertler (in [25]), with a spread parameter of 7.67, indicating a similar region based on mean flow velocity. Local Nusselt number distribution for an impinging slot jet at a $Re = 22{,}500$ for a nozzle spacing of 3.5 hydraulic diameters were compared with data from literature for a slot jet under similar Re and nozzle spacings. The present data were in fairly good agreement with those of Schlünder (in [1]), and indicated a maximum difference of 14% at a downstream location of $x/D_h = 4.0$ past impingement [23].

Uncertainties in reported data were calculated based on propagation of errors method [26] and are presented in Table 1. Uncertainties in mean flow velocity and fluctuating velocity variance were calculated at each measurement location. The velocity uncertainty estimate included errors due to the uncertainty in fringe spacing and the clock resolution of the processor. The uncertainties in the calculated quantities, U and $\langle uu \rangle$ were based on the component resolution equations, and were typically larger than those in the directly measured quantities (V and $\langle vv \rangle$). Uncertainties in the measured mean values were less than 3% in all cases, while that in $\langle uu \rangle$ was as large as 18% at near-wall locations. Heat transfer coefficient uncertainties were calculated for each data set, and included uncertainties in the heat loss compo-

Table 1
Uncertainty estimates in variables

Variable	Uncertainty
Mass flow rate, $\dot{m}$ (kg/s)	1.5%
Fluctuating velocity variance, $\langle uu \rangle$ for $Y_n/X_w = 0.25$ case (calculated quantity)	Maximum of 18% of local $\langle uu \rangle$, typically less than 10% in near-wall region
Fluctuating velocity variance, $\langle vv \rangle$ for $Y_n/X_w = 0.25$ case (measured quantity)	Maximum of 5% of local $\langle vv \rangle$, typically less than 3% in the near-wall region
Pressure coefficient	Typically less than 8.7% of $C_{p,\max}$
RMS surface fluctuating pressure (Pa)	Typically less than 10% of $\Delta P_{\mathrm{RMS},\max}$
Heat transfer coefficient, h_{loc} for $Y_n/X_w = 0.25$ case	Maximum of 11% of local value with an average of value of 2.9%
Pixel location uncertainty in temperature measurements	1.5% of 1 pixel value
Length scale, λ (for $Y_n/X_w = 0.25$ case)	17.6%
Nusselt number, Nu (for $Y_n/X_w = 0.25$ case)	13.8% of Nu_{loc} on average
ΔT_{ij} and θ_j	0.14 °C and 0.003, respectively

nents, electrical voltage and current, geometry, and measured foil temperature. The Nusselt number uncertainty also included the uncertainty due to the estimation of the length scale, λ.

3.2. Local heat transfer distribution

Fig. 3(a)–(d) present the variation in contours of time-averaged, spatially local heat transfer coefficient (h_{loc}) distribution with nozzle-to-surface-spacing and exit opening for the SJR flow at a $Re = 5000$. Fig. 3(a)–(c) depict contours at increasing nozzle-to-surface spacings of $Y_n/X_w = 0.25$, 0.50, and 0.75, respectively, at a fixed exit opening, $b/X_w = 0.10$. Fig. 3(d) and (a) represent contours for increasing exit openings of $b/X_w = 0.05$, and 0.10, respectively, at the closest nozzle-to-surface spacing, $Y_n/X_w = 0.25$. In all cases, reattachment was stronger at the circular ends of the nozzle compared to the rectangular region.

The distributions in Fig. 3(a)–(c) indicated that the variations in h_{loc} profiles in the rectangular region (parallel to the major axis of the nozzle) from a planar reattaching jet flow increased with nozzle-to-surface spacing. The low heat transfer rate corresponding to the contour line of 30 W/m^{2}K was restricted to $x/X_w \leqslant 0.6$ in Fig. 3(a). In contrast, the larger spacing cases in Fig. 3(b) and (c) indicate an outgrowth of the low heat transfer rate region in the x-direction around $z/X_w = 0.0$, with a corresponding reduction in its extent along the major axis (z-direction). This observation suggested the existence of a similar near-wall flow structure within the recirculation region for larger nozzle spacings that was distinct from that at the lowest spacing. Comparing the two cases with increasing exit openings (Fig. 3(d) and (a)), the extent of the low-heat-transfer region (following the 30 W/m^{2}K contour within the recirculation region) increased in the z-direction, while changing little along the x-direction. Thus, Fig. 3(a)–(d) indicated that the mean surface heat transfer coefficient distribution along the nozzle minor axis (x-direction) in the recirculation region varied predominantly with nozzle spacing.

For the SJR flow, disregarding the region beneath the bottom plate, it can be argued that a geometrically similar flow was attained by maintaining a fixed Y_n/b. However, as seen in Fig. 3(a)–(d), changes that occurred to the length scale, λ, due to flow variations in the geometrically non-similar part of the recirculating flow (the region beneath the nozzle plate) significantly altered the Nu distribution. Changes in the mean contours between the smallest nozzle-to-surface spacing of $Y_n/X_w = 0.25$ and the larger spacings in the recirculation region were most evident. Fig. 3(e), which represents the centerline ($z/X_w = 0.0$)Nu variation with x^* for two cases in Fig. 3(b)–(d), is one such example with identical $Y_n/b = 5$, but different Y_n and b. Note that the profiles along x-axis in the positive and negative directions intersected at $x^* = 0$ since the physical nozzle centerline, $x = 0.0$, corresponds to $x^* = \pm X_w/2\lambda$ (see Eq. (3)). A low nozzle spacing (Fig. 3(d)), corresponding to a small λ, provided high h_{loc}. In contrast, for the larger spacing (Fig. 3(b)), h_{loc} was low, but λ was large. For a dynamically similar flow, it is expected that a decrease in h_{loc} would compensate for the increase in λ, and the two Nu profiles presented in Fig. 3(e) would be identical. However, the outward spread at the nozzle centerline for the larger spacing, presumably caused due to differences in near-wall flow structure in the non-similar flow region beneath the bottom plate, resulted in an additional increase in λ, thereby enhancing Nu for the larger spacing over the lower spacing. Note that this increased λ mainly affected Nu, and less so the location of the non-dimensional reattachment distance, x_r^*, which remained identical for both cases shown in Fig. 3(e). A sensitivity index calculation on Nu equation indicated that Nu was 2.6 times more sensitive to variation in the reattachment location, x_r compared to the nozzle-to-surface spacing, Y_n. In contrast, a similar calculation on Eq. (2) indicated that x_r^* was on an average 2.6 times more sensitive to variations in Y_n compared to x_r for the same two cases. Thus, the outward spread at $z/X_w = 0.0$ along x^* that resulted from the non-similar flow region would have a significantly larger impact in altering Nu than x_r^*.

In the experiments reported by Narayanan et al. [22] for the 7.6:1 aspect ratio SJR nozzle, the closest nozzle-to-surface spacing was $Y_n/X_w = 0.57$. Therefore, it can be argued that in their experiments, a similar flow structure possibly existed at all spacings, and the λ scaling allowed for a reasonable collapse of Nu data for Y_n/b = constant. While the non-dimensional scheme outlined in Narayanan et al. [22] is acceptable for strictly two-dimensional offset jets, it can be used in only restricted situations for SJR flows where the flow structure in the recirculation region is expected to be identical for the two cases under comparison. Further evidence of the differences in flow structure with nozzle spacing will be apparent in the transient temperature data presented in the next section.

3.3. Transient surface visualization

Fig. 4(a)–(d) present variations in low-frequency differential thermal images of the impingement surface with nozzle-to-surface spacing for the SJR flow at $Re \approx 10{,}000$. The exit opening was fixed at $b/X_w = 0.10$. Eight consecutive thermal images were recorded at 1 frame/s and each image was then subtracted from the one previous to create a series of differential images. One such image from the series is presented in Fig. 4(a)–(d) for each of the four nozzle spacings studied. Note that since a line scanning imager was used, the images do not represent instantaneous snapshots of spatial temperature distribution. Consequently, the

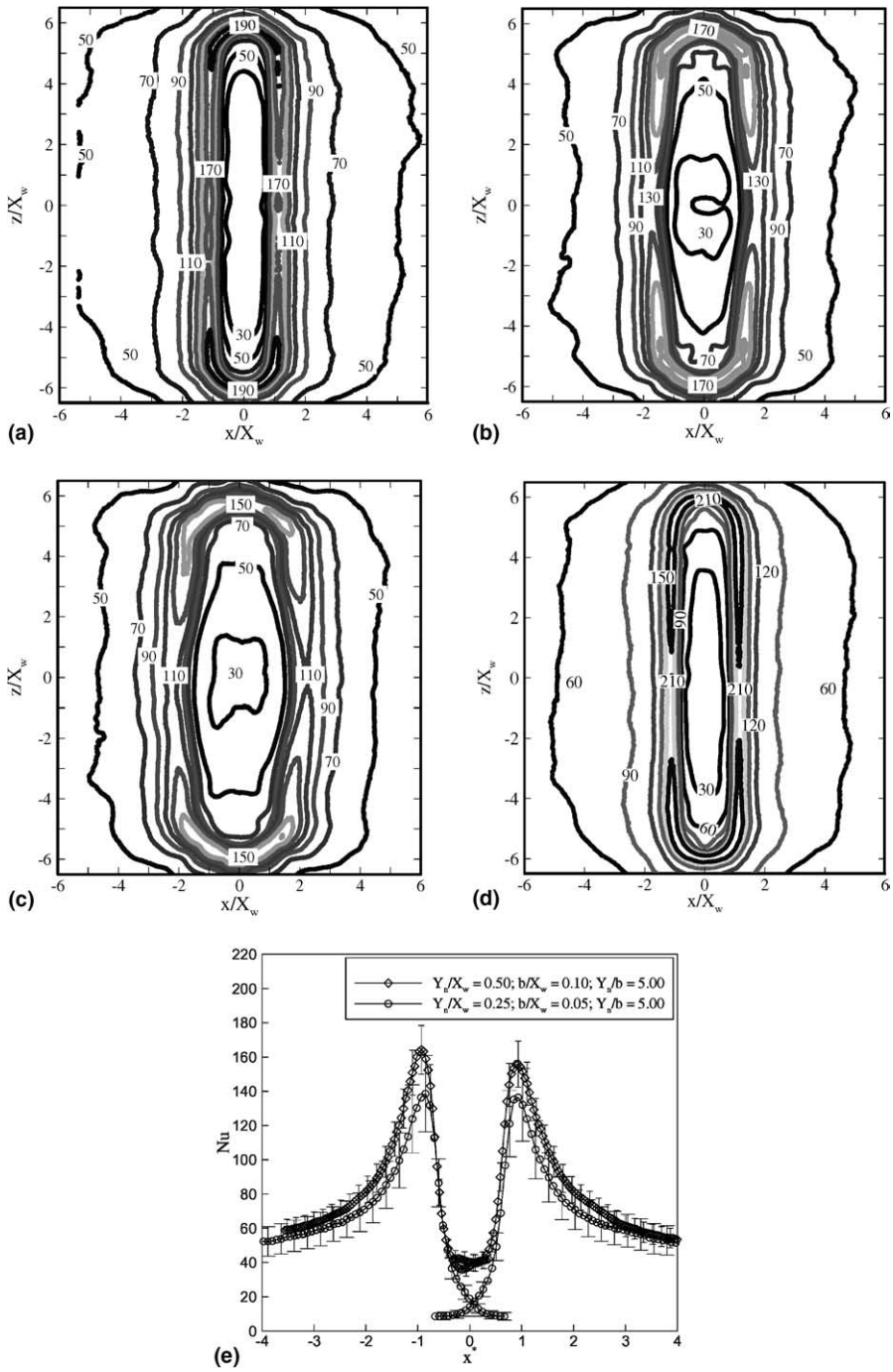

Fig. 3. (a)–(e) Local heat transfer rate distribution at $Re = 5000$; (a)–(d) Contour plots of h_{loc} (in W/m^{2}K): (a) $Y_n/X_w = 0.25$, $b/X_w = 0.10$, $Y_n/b = 2.5$; (b) $Y_n/X_w = 0.50$, $b/X_w = 0.10$, $Y_n/b = 5.0$; (c) $Y_n/X_w = 0.75$, $b/X_w = 0.10$, $Y_n/b = 7.5$; (d) $Y_n/X_w = 0.25$, $b/X_w = 0.05$, $Y_n/b = 5.0$; (e) Centerline ($z/X_w = 0.0$) Nu as a function of x^* for $Y_n/b = 5.0$ ((b) and (d)).

images could be spatially distorted; nevertheless, they represent low-frequency (1 Hz) differential temperature variations at each location. In the figures, the two solid lines on either side of the nozzle centerline represent the extent of the nozzle bottom plate. The dashed lines in Fig. 4(a) and (c) indicate the reattachment location that

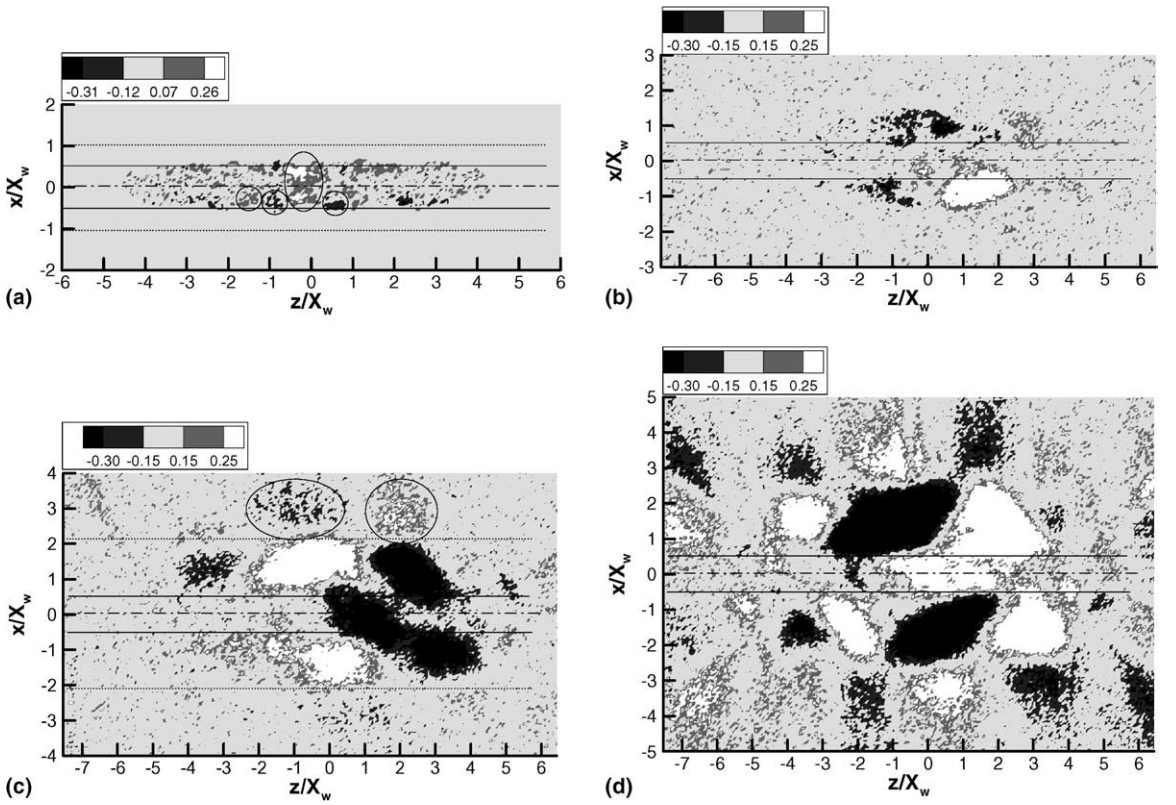

Fig. 4. (a)–(d) Differential thermal images of surface temperature variation (in °C) for the SJR flow, plotted as a function of nozzle-to-surface spacing for $Re = 10{,}000$, $b/X_w = 0.10$. (a) $Y_n/X_w = 0.25$; (b) $Y_n/X_w = 0.50$; (c) $Y_n/X_w = 0.75$; (d) $Y_n/X_w = 1.00$.

was identified from the mean flowfield measurements recorded at $z/X_w = 0.0$. Locations of alternating hot and cold (relative to the previous differential image) spots were identified in the recirculation region at all nozzle spacings. Such locations of differential temperatures could be interpreted as imprints of near-wall flow structures, and will henceforth be referred to as "thermal eddies".

In Fig. 4(a), the distribution outside $0.6 \leqslant x/X_w \leqslant 0.6$, which corresponded to the location of a large gradient in temperature, could not be obtained due to saturation of the detector. Within the recirculation region, alternating warm and cold thermal eddies (indicated by circles) were observed surrounding the nozzle bottom plate. The typical size of these eddies was approximately $0.4X_w$, and varied with exit opening and Re. Limited interaction between thermal eddies across the projected nozzle centerline ($x/X_w = 0.0$), restricted primarily to locations around z/X_w of 0.0, was observed. Mean flow field measurements in the recirculation region [27] at this spacing indicated the presence of a primary surface vortex with its center at $x/X_w = 0.90$, and $y/X_w = 0.04$ from the impingement surface. This vortex extended from $x/X_w = 0.75$ to the mean reattachment location at $x/X_w = 1.07$. Since the thermal eddies did not extend beyond $x/X_w = 0.75$ (this was clarified in similar cases without detector saturation) from the nozzle centerline for any exit opening or Re studied, it is clear that these eddies were distinct from the primary vortex. Thus, the flow structure within the recirculation region for the low spacing suggested the presence of a primary vortex with secondary three-dimensional eddies closer to the nozzle centerline.

For all nozzle spacings greater than $Y_n/X_w = 0.25$, (Fig. 4(b)–(d)) thermal eddies were observed in the entire recirculation region, and not restricted to areas near the nozzle bottom plate, indicating that the flow structure at these spacings were similar, but distinctly different from that at the closest spacing. For example, Fig. 4(c) presents a differential thermal contour for $Y_n/X_w = 0.75$ at $Re = 10{,}000$ and $b/X_w = 0.10$. The image suggests a highly three-dimensional near-wall flow with large-scale thermal eddies that scale with Y_n, distributed in recirculation region. Mean flow field along $z/X_w = 0.0$ for this spacing [27], measured at a slightly larger Re of 10,500 indicated that the primary vortex extended to approximately $x/X_w = 0.875$ in the recirculating flow, with the vortex center located at $x/X_w = 1.75$. In general, this

corresponded well with the location of the thermal eddies along $z/X_w = 0$, strongly suggesting that the hot and cold thermal spots in the region $0.6 \leqslant x/X_w \leqslant 2$ for the larger spacing represented an imprint of the primary surface vortex. It is also interesting to note that the thermal eddies were not uniform along the nozzle major axis (z-direction); this indicates spatial variations and a possible breakup of the primary vortex at large spacings. Secondary thermal eddies, and, in some cases, an interaction between the primary vortices on both sides of the nozzle centerline, were also observed underneath the nozzle plate.

In the developing flow past reattachment ($x/X_w > 2.15$), distinct low and high temperature regions (identified by oval highlights in Fig. 4(c)) were observed. These areas suggest a periodic flux of low or high temperature fluid in the near-wall region. The frequency associated with this phenomenon could not be measured using the low-frequency thermal images. In this study, similar low-frequency thermal "bursts" were not evident at the lower spacing of $Y_n/X_w = 0.25$ (as inferred from unsaturated images at larger Re). The bursts could be associated with a "sweeping" motion of the jet near reattachment, where there is an ejection of high temperature fluid from the recirculation region during breakup of the jet curtain, and entrainment of cooler ambient fluid on subsequent re-establishment of the jet curtain. The differential thermal image at the largest spacing (Fig. 4(d)) reiterates the flow observations discussed in regard to Fig. 4(c), with large thermal eddies within the recirculation region and dramatic hot and cold streaks past reattachment. Le et al. [20], in their DNS study of a low Re backstep, noticed saw-toothed temporal variation of the spanwise-averaged reattachment location. The rise of the reattachment length correlated well with the growth of large-scale roll-up of the shear layer prior to the step, and the following sudden reduction in length corresponded to the detachment of the large-scale structure from the step. Spanwise-averaged pressure fluctuations near reattachment location also indicated low frequency (Strouhal number of approximately 0.06) periodic behavior of the free shear layer. In addition to the temporal variations, instantaneous velocity fields indicated spanwise variation of the reattachment location.

Fig. 5(a)–(c) show time traces of instantaneous differential wall temperature, $\Delta T_{i,j}$ (Eq. (4)) along three locations parallel to the nozzle major axis for the $Y_n/X_w = 0.25$ and $b/X_w = 0.10$ SJR flow at a Re of 10,500. The first two locations were within the recirculation region, and corresponded to the projected nozzle major axis ($x/X_w = 0.0$) and $x/X_w = 0.71$. The latter closely corresponded to the location of interaction between the primary and secondary vortex structures within the recirculation region. The third time trace, measured at $x/X_w = 1.13$, corresponded to the reattachment region. The frame rate was 0.05 frames/s for the traces shown. The time trace at the centerline (Fig. 5(a)), indicates a band of lower differential temperature compared to its immediate surrounding around $z/X_w = 0.0$. The width of the band of approximately $0.4X_w$ was in good agreement with the dimensions of the interacting thermal eddies at $x = 0.0$ observed in Fig. 4(a). This band also exhibited low frequency temporal variations of temperature indicated by the light-gray central patches. Temporal variation at this location provides a measure of the interaction frequency of thermal eddies at the nozzle centerline (see Fig. 4(a)). Similar surface thermal traces and flow streaks near the surface have been reported in the stagnation region in an external flow around a cylinder [28], in rectangular duct flows [29], and in impinging jet flows [30,31]. They are generally attributed to the presence of orderly near-wall flow structures. Van Fossen and Simoneau [28] performed both near-wall and surface flow visualization to identify a relation between the near-wall counter-rotating vortices and the wall temperature variations along the stagnation line of a cylinder. Yokobori et al. [30] studied the near-wall flow in an impinging slot jet, by performing flow visualization, and identified streamwise aligned counter-rotating vortices along the stagnation line. They suggested that these vortices were responsible for the enhanced heat transfer in the region. More recently, Sakakibara et al. [31] quantitatively visualized the near-wall fluid flow and temperature simultaneously along the stagnation line in an impinging slot jet to establish a relation between near-wall vortices and fluid temperature.

Fig. 6(a) presents the plots of the non-dimensional RMS temperature fluctuations, θ_j, calculated using Eq. (5), for the three time traces shown in Fig. 5(a)–(c). Since only 1648 data points could be recorded continuously at any frame rate, data were recorded at two frame rates of 0.05 and 0.017 frames/s to identify the effect of sampling duration on the results. The RMS fluctuations calculated using both frame rates were in good agreement, indicating that the recording time at 0.05 frames/s was sufficient to capture the low frequency fluctuations observed in this flow. At the centerline, the level of RMS fluctuation was low except around $z/X_w = 0.0$, where it attained a maximum value. Fig. 5(b) shows the time trace recorded at $x/X_w = 0.71$, and Fig. 6(a) plots the corresponding RMS temperature fluctuations. At this location, many more thermal streaks at stable locations were observed. The presence of bands of width approximately $0.4X_w$ suggested the persistence of eddies that were observed in the vicinity of the nozzle plate in Fig. 4(a) at $x/X_w = 0.71$. The mean heat transfer contours in Fig. 3(a) (also see centerline h_{loc} distribution in Fig. 7(a)) indicated that this location corresponded to the beginning of the steep rise in heat transfer toward the peak at reattachment. Figs. 5(c) and 6(a) show a time-trace and the corresponding RMS temperature

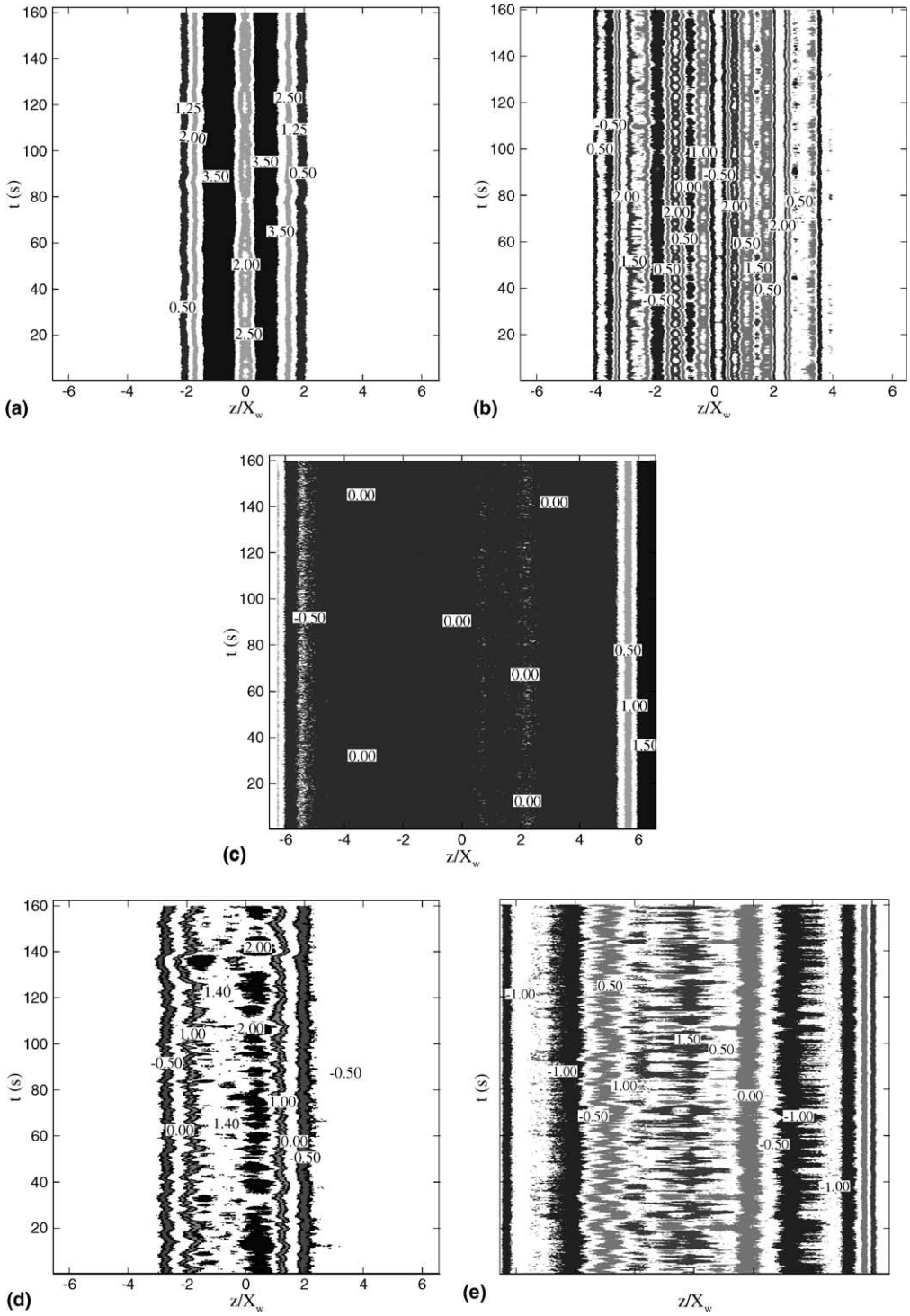

Fig. 5. (a)–(e) Time traces of surface temperature for SJR flow. Legends indicate $\Delta T_{i,j}$ in °C. (a)–(c) $Y_n/X_w = 0.25$, $Re = 10{,}500$, $b/X_w = 0.10$: (a) $x/X_w = 0.0$; (b) $x/X_w = 0.71$; (c) $x/X_w = 1.07$. (d)–(e) $Y_n/X_w = 0.75$, $Re = 10{,}500$, $b/X_w = 0.10$: (d) $x/X_w = 0.0$; (e) $x/X_w = 1.49$.

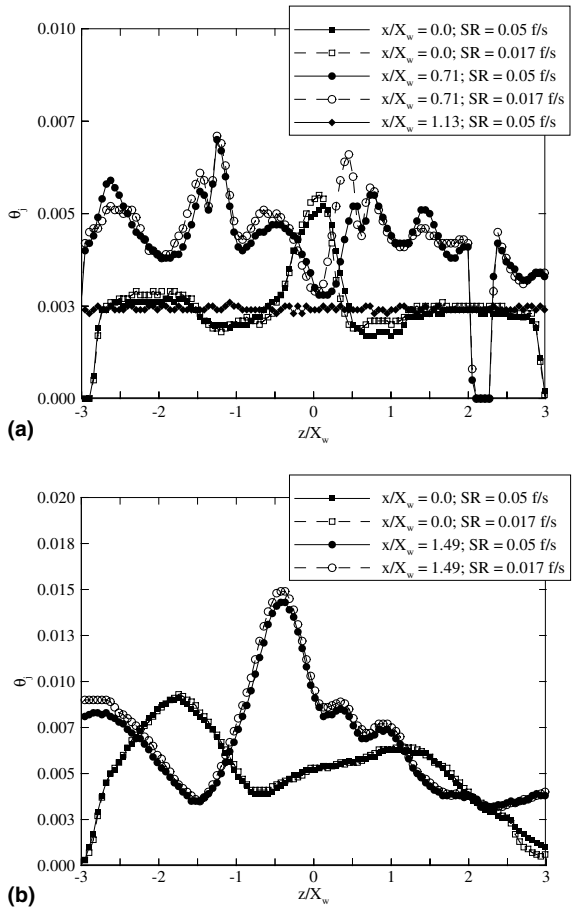

Fig. 6. (a)–(b) RMS surface temperature variation corresponding to time trace in (a) Fig. 5(a)–(c) and (b) Fig. 5(d) and (e).

fluctuation, respectively, at a location slightly past reattachment ($x/X_w = 1.13$). No distinct bands of temperature were observed, indicating the absence of low-frequency (less than 10.35 Hz) thermal transients at this location.

Fig. 5(d) and (e) show time traces at two locations in the recirculation region, $x/X_w = 0.0$ (centerline) and $x/X_w = 1.49$, for the SJR flow at $Y_n/X_w = 0.75$ and $Re = 10{,}500$. The RMS temperature fluctuations corresponding to these time traces are plotted in Fig. 6(b). The RMS fluctuations along the z-direction observed at this nozzle spacing were, in general, larger than at lower spacing for both time-trace locations. The higher centerline mean heat transfer coefficient observed for the larger nozzle spacing suggested that the reduced region of low heat transfer along the z-direction in the recirculation region near the nozzle plate (Fig. 3) with increase in nozzle spacing was related to the increased near-wall flow unsteadiness. The location $x/X_w = 1.49$ represented the approximate center of the large thermal structures associated with the primary vortex in the recirculation region, and corresponded to a region of general rise in mean heat transfer coefficient.

3.4. Near-wall turbulence, surface pressure, and heat transfer

This section presents the results of near-wall fluid mechanics and mean heat transfer rate along the minor axis centerline, $z/X_w = 0.0$, for the two nozzle spacings of $Y_n/X_w = 0.25$ and 0.75 discussed in the previous section. The recirculation region and a high heat transfer region that corresponds approximately to the reattachment region are discussed. Fig. 7(a) and (b) present the composite plots of mean heat transfer coefficient, non-dimensional surface pressure, C_p, normalized RMS averaged surface pressure fluctuations, and normalized streamwise and normal velocity fluctuation variance for $Y_n/X_w = 0.25$ and 0.75 SJR flows, respectively. The velocity fluctuation variances reported here were measured at $y/X_w = 0.02$ from the impingement surface.

3.4.1. Recirculation region

Flow measurements in the vicinity of the nozzle up to $x/X_w = 0.75$ could not be performed due to obstruction of the beam path by the nozzle. Hence, a combination of temperature–time trace and surface pressure measurements will be used to interpret the near-wall flow field and its effect on heat transfer rate up to $x/X_w = 0.75$. The mean pressure was almost constant and sub-atmospheric in this region at both nozzle spacings, with its absolute value being smaller for the larger spacing. The RMS pressure fluctuations were low up to $x/X_w = 0.65$ for the lower nozzle spacing, and up to $x/X_w = 0.88$ for the larger nozzle spacing. For the larger nozzle spacing, the mean heat transfer coefficient was also low and remained fairly constant at 52 W/m^2K up to $x/X_w \approx 0.9$. In contrast, for the lower spacing, the mean heat transfer coefficient gradually increased from a low of 24 W/m^2K at the centerline to 110 W/m^2K at $x/X_w = 0.71$. Beyond $x/X_w = 0.75$, the gradient of heat transfer coefficient increased rapidly towards its peak value near reattachment. The transient thermal images presented in the previous section explain these mean heat transfer trends well. For the larger nozzle spacing, a combined effect of the proposed periodic breakdown of reattachment curtain and the large thermal eddies (Fig. 4(c)) observed near the centerline could have resulted in a relatively large but constant mean heat transfer coefficient in the $x/X_w < 0.85$ region. Mean velocity measurements along the nozzle centerline, $z/X_w = 0.0$, indicated that the primary recirculation surface vortex extended up to $x/X_w = 0.88$. As mentioned before, this location corresponded well with the extent of the thermal eddies along $z/X_w = 0.0$ and suggested that the rise in mean heat transfer beyond $x/X_w = 0.875$ occurred due to the presence of the primary vortex. For the lower

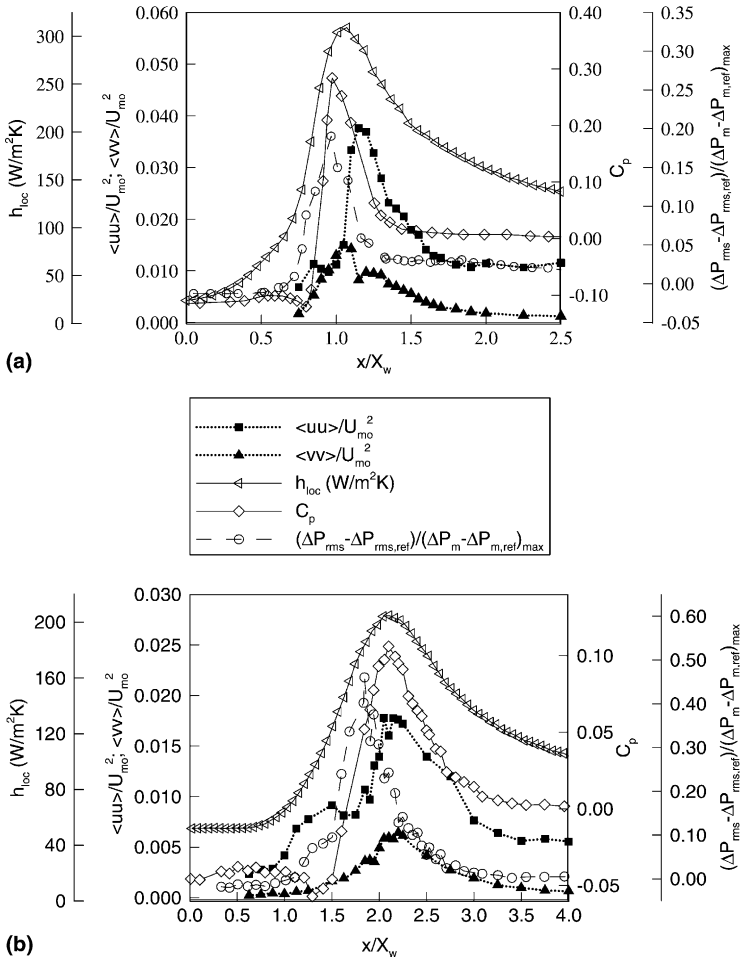

Fig. 7. Combined heat transfer, surface pressure and near-wall ($y/X_w = 0.02$) velocity variance profiles for the SJR flow at $Re = 10{,}500$. (a) $Y_n/X_w = 0.25$, $b/X_w = 0.10$; (b) $Y_n/X_w = 0.75$, $b/X_w = 0.10$.

nozzle spacing, there was an occasional interaction of thermal eddies along $z/X_w = 0.0$ (Fig. 4(a)), with a more consistent presence of thermal eddies immediately surrounding the nozzle centerline up to $x/X_w = 0.7$, which resulted in a steady increase in heat transfer coefficient. Mean velocity measurements [27] indicated that the primary vortex extended from $x/X_w = 0.75$ to 1.0, corresponding to the region of rising heat transfer coefficient with a steep gradient.

For the $Y_n/X_w = 0.75$ SJR flow, the extent of the primary vortex corresponded well with the region of increasing heat transfer, surface pressure fluctuations, and near-wall $\langle uu \rangle$. The peak pressure fluctuation in the recirculation region occurred at $x/X_w = 1.85$, with a large magnitude of 46% of the maximum mean pressure. This location corresponded very well with the high $\langle vv \rangle$ region in the lower shear layer of the reattaching jet above the primary recirculation vortex and suggested the possibility of periodic breakup and re-formation of the reattachment curtain. Pelfrey and Liburdy [13] noticed an enhancement of $\langle vv \rangle$ and suppression of $\langle uu \rangle$ in the lower shear layer (concave side) of the offset jet. A small rise in the near-wall $\langle uu \rangle$, followed by a plateau, occurred within the recirculation region. Its location, at $x/X_w = 0.85$ and 1.50 for $Y_n/X_w = 0.25$ and 0.75 flows, respectively, coincided fairly well with that of peak negative pressure in the recirculation region. Such an increase in near-wall $\langle uu \rangle$ has not been explicitly reported for offset jets. The cause for this rise in $\langle uu \rangle$ is unclear.

3.4.2. High heat transfer region

For purposes of discussion in this section, the region of high heat transfer refers to the location where the heat transfer coefficient varies by less than 5% of its peak value. For the lower spacing, this region corresponded to $0.95 \leqslant x/X_w \leqslant 1.15$, and the peak heat transfer coefficient occurred at $x/X_w = 1.07 \pm 0.06$. A zero near-wall

mean streamwise velocity occurred at $x/X_w = 1.05$ indicating the reattachment point. The near-wall $\langle vv \rangle$ also peaked at this location, and its magnitude of $\langle vv \rangle / U_{mo}^2 = 0.015$ was 2.5 times larger than for the larger nozzle spacing. Near-wall $\langle uu \rangle$ peaked further downstream at $x/X_w = 1.15$ with a much larger magnitude than $\langle vv \rangle$. The mean and RMS pressure peaked at $x/X_w \approx 1.0$, slightly ahead of reattachment and peak heat transfer location. The collocation of peak h_{loc}, and near-wall $\langle vv \rangle$, at the attachment point strongly suggested an intermittent impingement of the jet at reattachment to be one of the mechanisms for enhanced heat transfer. The generally high value of $\langle vv \rangle$ in the lower shear layer of the jet, and the high RMS surface pressure fluctuation that peaked at $x/X_w = 1.0$ indicated unsteadiness in the flow at attachment. However, at this nozzle spacing, no evidence of low-frequency flapping (<10.35 Hz) was visible in the thermal time traces shown in Fig. 5(c). Further transient studies at higher frequencies are necessary to determine if a periodic breakdown of the reattachment curtain occurred at higher frequencies for the lower spacing, or if periodic outbursts were not observed due to a stronger jet attachment.

For the larger nozzle spacing SJR flow, the peak heat transfer occurred at $x/X_w = 2.11 \pm 0.06$. The extent of the high heat transfer region, in this case, defined using the same criterion, was $1.95 < x/X_w < 2.25$. Peak C_p and near-wall $\langle vv \rangle$ occurred close to the peak heat transfer location. However, peak C_p was 2.7-times, and peak $\langle vv \rangle$ 2-times lower than for the lower nozzle spacing. The peak near-wall $\langle uu \rangle$ was 2.7-times larger than peak $\langle vv \rangle$ and also corresponded well with the location of peak heat transfer, indicating the dominant role of $\langle uu \rangle$ in heat transport in the reattachment region at this spacing. The high $\langle vv \rangle$ observed in the lower shear layer of the attaching jet, coupled with a lower mean C_p (compared to the lower nozzle spacing) suggested a weak attachment, and were indicators of a periodic breakup of the reattachment curtain. This periodic breakup might have resulted in the observed high near-wall $\langle uu \rangle$ and enhancement in heat transfer rate at this location. Vogel and Eaton [17] found that the fluctuating skin friction controlled the heat transfer rate in the reattachment region of the backward-facing-step flow.

The contribution of turbulence to heat transfer in the high heat transfer region was determined by the ratio of the average near-wall turbulence kinetic energy in this region, normalized by the mean flow exit kinetic energy, to the average C_p. Results indicated this ratio to be 13.4% for the lower spacing, and 22.6% for the larger spacing. This estimate highlights the increasing role of turbulence in heat transport in the reattachment region for larger nozzle spacings.

The location of peak heat transfer was determined to be a constant at $x_r^* = 0.91$. This compares favorably with $x_r^* = 0.933$ for the 7.6:1 aspect ratio SJR nozzle study, and $x_r^* = 0.88$ for the offset jet. The lower x^* compared to the 7.6:1 aspect ratio nozzle can be attributed to the different aspect ratios and nozzle exit conditions of the jets in the studies. A higher x_r^* compared to the offset jet could, in addition to the above, be due to the effect of the non-similar flow region in reattachment jets. In this study, the peak (reattachment) Nu was correlated to Re, Y_n/b, and b/X_w by

$$\frac{Nu}{Re^{0.615}} = A \cdot \left(\frac{Y_n}{b}\right)^B \left(\frac{b}{X_w}\right)^C \tag{6}$$

where $A = 0.839$, $B = 0.507$, and $C = 0.353$. This correlation is valid in the range of $5000 \leqslant Re \leqslant 15{,}000$, $1.66 \leqslant Y_n/b \leqslant 20$, $0.25 \leqslant Y_n/X_w \leqslant 1.00$, and $0.05 \leqslant b/X_w \leqslant 0.15$, for a 20:1 SJR exiting parallel to the impingement surface. A combination of Y_n/b and b/X_w permitted the inclusion of the effects of nozzle spacing and exit opening in the non-similar flow region beneath the nozzle bottom plate onto the similar region of the flow. Note that the exponent of 0.615 for Re was significantly different from the 0.7 power for the 7.6:1 aspect ratio SJR study [22]. This difference is attributed primarily to the different aspect ratios of the jet between the two studies. Circular jet impingement Nu correlations at the stagnation point (for example [32]) have reported exponents of 0.76 power for Re, while those for slot jets [18] have indicated a 0.58 power dependence. Vogel and Eaton [16] reported a 0.6 power dependence of Re on Nu in heat transfer studies for a backward facing step geometry. Fig. 8 plots the predicted $Nu_{max}/Re^{0.615}$ trends with the experimental data as a function of Y_n/b for various exit openings, b/X_w. Clearly, there is significantly larger scatter of data at the lowest nozzle spacing. It is also apparent that Nu data do not collapse for a fixed Y_n/b

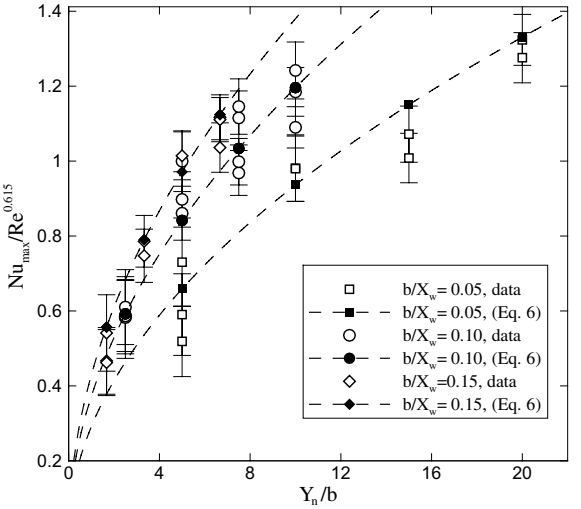

Fig. 8. Comparison of experimental Nu_{max} and correlation (Eq. (6)) prediction for SJR flow.

(for example, $Y_n/b = 5$ and 10) for any combination of Y_n/X_w or b/X_w, which can be attributed to the differences in flow in the non-similar region, as discussed previously in relation to Fig. 3.

4. Conclusions

Detailed mean and transient surface temperature and pressure, and near wall flow measurements for a reattaching slot jet flow were presented for two nozzle spacings of 0.25 X_w and 0.75 X_w, where X_w corresponded to the width of the nozzle bottom plate. The flow structure in the recirculation region was examined using low-frequency differential surface temperature measurements and time traces along specific locations on the surface. Thermal flow structures (called "thermal eddies") were identified in the recirculation region at both nozzle spacings. While large thermal flow eddies existed throughout the recirculation region for the larger spacing, they were restricted predominantly to a band between $x/X_w = 0.4$ and 0.75 at the lower spacing with few instances of interaction at the centerline, limited to $-1 < z/X_w < 1$ for the case presented.

The high heat transfer rate was attributed to the high near-wall velocity fluctuation variances that peaked near reattachment for both spacings. For the lower nozzle spacing, a high normal variance, $\langle vv \rangle$, suggested that an intermittent impingement caused the enhanced heat transfer. No low-frequency (<10.35 Hz) temperature fluctuations at reattachment were observed to corroborate this intermediate impingement hypothesis; however, fluctuations might have existed at higher frequencies.

For the larger spacing, the high near-wall streamwise fluctuating velocity variance correlated well with heat transfer. Low-frequency differential thermal images showed the presence of hot and cold streaks outside the reattachment region, suggesting the ejection of warm fluid from, and entrainment of cool ambient fluid into the recirculation region. This observation, coupled with the high $\langle vv \rangle$ in the lower jet shear layer indicated a possible periodic breakdown of the reattachment curtain at these spacings. Such streaks were not detected for the lower spacing. The contribution of near-wall turbulence to heat transfer in the reattachment region was shown to be significant, especially at larger nozzle spacings. A correlation for peak Nu that accounted for the non-similar region effects was provided in terms of the nozzle geometrical parameters.

Acknowledgment

The authors acknowledge the financial support provided by the Texas A&M Drying Research Center and the equipment support provided by NASA.

References

[1] H. Martin, Heat and mass transfer between impinging gas jets and solid surfaces, Adv. Heat Transfer 13 (1977) 1–60.
[2] R. Viskanta, Heat transfer to impinging isothermal gas and flame jets, Exp. Thermal Fluid Sci. 6 (1993) 111–134.
[3] L. Huang, M.S. El-Genk, Heat transfer and flow visualization experiments of swirling, multi-channel, and conventional impinging jets, international, J. Heat Mass Transfer 41 (3) (1998) 583–600.
[4] J. Lee, S.-J. Lee, The effect of nozzle aspect ratio on stagnation region heat transfer characteristics of elliptic impinging jet, Int. J. Heat Mass Transfer 43 (2000) 555–575.
[5] R.H. Page, L.L. Hadden, C. Ostowari, A theory for radial jet reattachment flow, AIAA J. Thermophys. Heat Transfer 27 (11) (1988) 1500–1505.
[6] J. Seyed-Yagoobi, Enhancement of heat and mass transfer with innovative impinging jets, Drying Technol. 14 (5) (1996) 1173–1196.
[7] J. Seyed-Yagoobi, V. Narayanan, R.H. Page, Comparison of heat transfer characteristics of radial jet reattachment nozzle to in-line impinging jet nozzle, ASME J. Heat Transfer 120 (1998) 335–341.
[8] J.W. Mohr, J. Seyed-Yagoobi, R.H. Page, Heat transfer characteristics of a radial jet reattachment flame, ASME J. Heat Transfer 119 (1997) 258–264.
[9] J. Wu, J. Seyed-Yagoobi, R.H. Page, Heat transfer and combustion characteristics of an array of radial jet reattachment flames, J. Combust. Flame 125 (2001) 955–964.
[10] K. Bremhorst, N.D. Agnew, Surface heat transfer and flow structures of steady and fully pulsed radial reattaching jets, Int. J. Heat Fluid Flow 20 (1999) 280–289.
[11] J. Seyed-Yagoobi, R.H. Page, M.C. Asensio, E.W. Thiele, Enhancement of drying rate in paper machines with multifunctional radial jet reattachment blow boxes—Theoretical analysis, in: Proceedings of the Ninth International Drying Symposium, Gold Coast, Australia, 1994, pp. 661–666.
[12] J.R.R. Pelfrey, J.A. Liburdy, Mean flow characteristics of a turbulent offset jet, ASME J. Fluids Eng. 108 (1985) 82–88.
[13] J.R.R. Pelfrey, J.A. Liburdy, Effect of curvature on the turbulence of a two-dimensional jet, Exp. Fluids 4 (1986) 143–149.
[14] A. Nasr, J.C.S. Lai, A turbulent plane offset jet with small offset ratio, Exp. Fluids 24 (1998) 47–57.
[15] J.K. Eaton, J.P. Johnston, A review of research on subsonic turbulent flow reattachment, AIAA J. Thermophys. Heat Transfer 19 (9) (1981) 1093–1100.
[16] J.C. Vogel, J.K. Eaton, Heat transfer and fluid mechanics measurements in the turbulent reattaching flow behind a backward-facing step, Report MD-44, Thermosciences Division, Department of Mechanical Engineering, Stanford University, Stanford, California, 1984.
[17] J.C. Vogel, J.K. Eaton, Combined heat transfer and fluid dynamic measurements downstream of a backward-facing step, ASME J. Heat Transfer 107 (1985) 922–929.
[18] M. Kumada, I. Mabuchi, K. Oyakawa, Generalized correlation of mass transfer by reattached jet at stagnation point on a plate, Heat Transfer- Jap. Res. 3 (1974) 93–104.

[19] K. Abe, T. Kondoh, Y. Nagano, A new turbulence model for predicting fluid flow and heat transfer in separating and reattaching flows—I. Flow field calculations, Int. J. Heat Mass Transfer 37 (1) (1994) 139–151.
[20] H. Le, P. Moin, J. Kim, Direct numerical simulation of turbulent flow over a backward-facing step, J. Fluid Mech. 330 (1997) 349–374.
[21] S. Jovic, D.M. Driver, Reynolds number effect on the skin friction in separated flows behind a backward-facing step, Exp. Fluids 18 (1995) 464–467.
[22] V. Narayanan, J. Seyed-Yagoobi, R.H. Page, Heat transfer characteristics of a slot jet reattachment nozzle, ASME J. Heat Transfer 120 (1998) 348–356.
[23] V. Narayanan, J. Seyed-Yagoobi, R.H. Page, Combined fluid mechanics and heat transfer measurements in normally impinging slot jet flows, Int. J. Heat Mass Transfer 47 (2004) 1827–1845.
[24] S.E. Logan, A laser velocimeter for Reynolds stress and other turbulence measurements, AIAA J. Thermophys. Heat Transfer 10 (7) (1972) 933–935.
[25] N. Rajaratnam, Turbulent Jets—Developments in Water Science 5, Elsevier Publishing Company, New York, NY, 1976.
[26] R.J. Moffat, Describing uncertainties in experimental results, Exp. Thermal Fluid Sci. 1 (1988) 3–17.
[27] V. Narayanan, An experimental flow field and heat transfer investigation of submerged double-sided reattachment and two-dimensional impingement slot jets, Ph.D. dissertation, Texas A&M University, College Station, TX, 2001.
[28] G.J. VanFossen, R.J. Simoneau, A study of the relationship between free-stream turbulence and stagnation region heat transfer, ASME J. Heat Transfer 109 (1987) 10–15.
[29] A. Mosyak, E. Pogrebnyak, G. Hestroni, Effect of constant heat flux boundary condition on wall temperature fluctuations, ASME J. Heat Transfer 123 (2001) 213–218.
[30] S. Yokobori, N. Kasagi, M. Hirata, N. Nishiwaki, Role of large-scale eddy structure on enhancement of heat transfer in stagnation region of two-dimensional, submerged, impinging jet, in: Proceedings of the Sixth International Heat Transfer Conference 5, Toronto, Canada, 1978, pp. 305–310.
[31] J. Sakakibara, K. Hishida, M. Maeda, Vortex structure and heat transfer in the stagnation region of an impinging plane jet, Int. J. Heat Mass Transfer 40 (13) (1997) 3163–3176.
[32] R.J. Goldstein, A.I. Behbahani, K.K. Heppelmann, Streamwise distribution of recovery factor and the local heat transfer coefficient to an impinging circular air jet, Int. J. Heat Mass Transfer 29 (8) (1986) 1227–1235.